Article

An Experimental- and Simulation-Based Evaluation on the CO Utilization Efficiency in Aqueous-based Electrochemical CO Reduction Reactors with Ion-Selective Membranes

Meng Lin, Lihao Han, Meenesh R. Singh, and Chengxiang Xiang

Just Accepted

An Experimental- and Simulation-Based Evaluation on the CO$_2$ Utilization Efficiency in Aqueous-based Electrochemical CO$_2$ Reduction Reactors with Ion-Selective Membranes

Meng Lin,[a, b†] Lihao Han,[a,b†] Meenesh R. Singh,[c] Chengxiang Xiang[a, b*]*

[a]*Joint Center for Artificial Photosynthesis, and Division of Chemistry and Chemical Engineering, California Institute of Technology, Pasadena, California 91125, United States*

[b]*Division of Chemistry and Chemical Engineering, California Institute of Technology, Pasadena, CA 91125, USA*

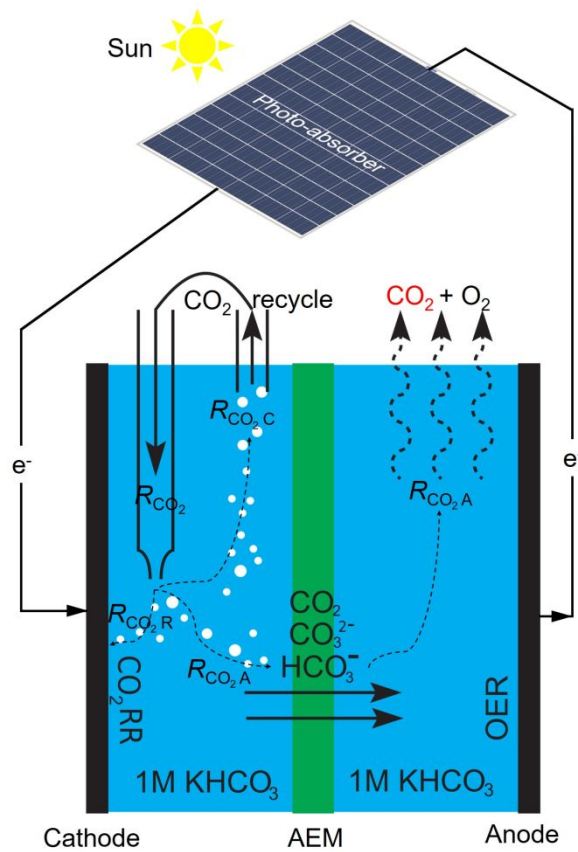[c]*Department of Chemical Engineering, University of Illinois at Chicago, Chicago, Illinois 60607*

*To whom correspondence should be addressed: cxx@caltech.edu, mrsingh@uic.edu

† Meng Lin and Lihao Han contributed equally to this work.

ABSTRACT

The CO_2 utilization efficiency of three types of electrochemical CO_2 reduction (CO_2R) reactors using different ion-selective membranes, including anion exchange membrane (AEM), cation exchange membrane (CEM), and bipolar membrane (BPM), was studied quantitively via both experimental and simulation methods. The operating current density of the CO_2R reactors was chosen to be between $10 - 50$ mA cm^{-2} to be relevant for solar-fuel devices with relatively low photon flux from sunlight. In the AEM based CO_2R reactor with a 6-electron per carbon CO_2R at the cathode surface, an upper limit of 14.4% for the CO_2 utilization efficiency was revealed by modeling and validated by experimental measurements in CO_2 saturated aqueous electrolytes without any buffer electrolyte. Improvements in CO_2 utilization efficiency were observed when additional buffer electrolyte was added into the aqueous solution, especially in solutions with low bicarbonate concentrations. The effects of the feed rate of the input CO_2 stream, the Faradaic Efficiency (FE) and the participating electron numbers of the cathode reaction on the CO_2 utilization efficiency was also studied in the AEM based CO_2R reactor. The CEM based CO_2R reactor exhibited low CO_2 utilization efficiency with re-circulation between the catholyte and the anolyte, and was unsustainable due to the cation depletion from the anolyte without any re-circulation. The BPM based CO_2R reactor operated continuously without a significant increase in the cell voltage and exhibited significantly higher CO_2 utilization efficiency, up to 61.4%, as compared to the AEM based CO_2R reactors. Diffusive CO_2 loss across the BPM resulted in relatively low CO_2 utilization efficiency at low operating current densities. Modeling and simulation also provided target BPM properties for higher CO_2 utilization efficiency and efficient cell operation.

1
2
3
4
5
6
7
8
9
10
11
12
13
14
15
16
17
18
19
20
21
22
23
24
25
26
27
28
29
30
31
32
33
34
35
36
37
38
39
40
41
42
43
44
45
46
47
48
49
50
51
52
53
54
55
56
57
58
59
60

TOC GRAPHICS

3

INTRODUCTION

Electrochemical and photoelectrochemical (PEC) CO_2 reduction (CO_2R) into value-added fuels or chemicals have become an active area of research in the past few years.[1–9] Significant advances have been made in the materials discovery and device architecture for selective and efficient CO_2R reactions.[3,10–15] In aqueous based CO_2R systems, ion selective membranes, such as cation exchange membrane (CEM), anion exchange membrane (AEM) or bipolar membrane (BPM), have been widely used to minimize the product crossovers and to provide ionic conductions between the cathode and anode chambers. In particular, the bipolar membrane-based reactors have been of significant interests[16–20] due to its ability to maintain pH differentials between the cathode and the anode chambers. Solar-driven CO_2 reduction devices that used bipolar membrane exhibited solar-to-fuel (STF) conversion efficiencies that exceeded 10% for CO generation[21] and for formate generation[22]. AEM-based solar-driven CO_2 reduction devices have also shown promising conversion efficiency to oxygenate and hydrocarbons[23,24] On the modeling side, although there have been several studies[25–27] on the effects of local pHs and local CO_2 concentrations on the operating conditions and constraints for CO_2R reactors, the CO_2 utilization efficiency is often overlooked or sacrificed in fundamental studies and in the materials discovery research in order to maintain a well-controlled reaction environment with constant CO_2 concentrations[28]. However, the utilization efficiency will have a significant impact on the overall efficiency of the system and the cost of the produced fuels or chemicals in practical devices. This study focuses on the analysis of the CO2 utilization behavior of membrane-based reactors. More specifically, the rate of CO2 crossover to the anode chamber and the CO2 utilization efficiency were modeled, simulated and experimentally measured in aqueous-based electrochemical devices with cation exchange membranes (CEMs), AEMs and bipolar

membranes (BPMs), and a range of electrolyte conditions. The simulation and the experimental results revealed significant challenges in improving the CO_2 utilization efficiency in aqueous-based configurations, especially with higher-electron CO_2R products.

RESULTS AND DISCUSSION

Fig. 1a shows the pathways of CO_2 transport in a generic aqueous-based electrochemical CO_2R device, in which the cathode for CO_2R reaction and the anode for oxygen evolution reaction (OER) are separated by an anion exchange membrane (AEM) separator that facilitates the ionic transport between the catholyte and anolyte. The CO_2 utilization efficiency (η_{CO_2}), which is defined as the CO_2 utilized per unit amount of CO_2 fed to the utilization process,[24] and can be written as the following:

$$\eta_{CO_2} = \frac{R_{CO_2R}}{R_{CO_2R} + R_{CO_2A} + R_{CO_2C}} \times 100\ \% \qquad (1),$$

where R_{CO_2C} is the rate of the un-reacted CO_2 leaving the cathode chamber, $R_{CO_2R} = \frac{\eta_F j_{total}}{nF}$ is the rate of CO_2R reaction at the cathode surface (n is the number of electrons participating in CO_2R reaction, F is the Faraday constant, j_{total} is the total geometric current density of the cathode, and η_F is the Faradaic efficiency for CO_2R reaction), and R_{CO_2A} is the rate of the CO_2 loss across the separator to the anode chamber in the form of CO_2, HCO_3^-, and CO_3^{2-}. $R_{CO_2} = R_{CO_2R} + R_{CO_2A} + R_{CO_2C}$ is the total rate of CO_2 feed to the cathode chamber. All the rates in Eq. 1 are normalized with respect to the unit area of the cathode. While the rate of the un-reacted CO_2 leaving the cathode chamber can be optimized and minimized in principle with multi-pass reactor designs, the CO_2 transported across the separator (R_{CO_2A}) would eventually co-evolve with O_2 from the anode and would result in significant energy penalties to bring O_2-free, relatively pure stream of

CO_2 back to the cathode. The R_{CO_2A} was measured experimentally and evaluated computationally in this study.

In the AEM-based CO_2R reactor (Fig. 1a), the CO_2 transport across the separator, the electrolyte concentrations and the resulting upper limit for the CO_2 utilization efficiency are independent of the overpotential of cathodic reaction. The generation rate of OH^- at the cathode electrode, which controls the electrolyte composition in the cathode chamber, is independent of the cathodic reaction, and is only determined by the operating current density of the electrode. As a result, as long as the catholyte is saturated with CO_2, the rate of HCO_3^- crossing through the AEM is independent of the cathodic reactions. The effect of cathodic reactions on R_{CO_2A} is shown in figure S1 showing no difference in R_{CO_2A} between CO_2R reaction with unity Faradaic efficiency and the hydrogen evolution (HER) case. Therefore, Ni cathode was used for HER, instead of CO_2R, to mimic the pH gradient and OH^- generation rate in the system as well as to simplify the experimental measurements and validations. This is implemented for all the experiments performed in this study. Furthermore, the electrochemical rates for the hydroxide generation and proton generation at the surface of the cathode and anode were held constant during the modeling and experimental measurements. While the concentration increase of CO_2R products during the reaction would change the equilibrium potential of the reaction, the electrode potential would be adjusted accordingly to maintain the constant operating current density. The anolyte was pre-bubbled with CO_2 gas without any circulation or stirring to ensure an initial equilibrium of the anolyte, AEM, and catholyte. The plasticization of membranes was not observed during the course of the measurements. Furthermore, the stable cell potential in AEM- (Figure S2c) and BPM-based (Figure S8c) reactors confirms the ionic properties of membranes were not changing significantly throughout the experiment. The lower range of operating current density- 10 - 50

mA cm^{-2}, chosen in this study to evaluate CO_2 utilization efficiency of the device, is comparable

to the operating photocurrent density of a solar-driven CO_2R system (without solar

concentration).[21–24,29–31] This will offer direct design guidelines for solar-driven CO_2R reactors

using various un-concentrated photo-absorbers.

In the AEM-based CO_2R reactor, the HCO_3^- was the dominating ionic current carrier crossing

the separator, which can be confirmed from Fig. S2b showing that the HCO_3^- cross-over current

density, $j_{HCO_3^-}$, was 9.9 mA cm^{-2} at the operating current density of 10 mA cm^{-2}. The crossed-

over HCO_3^- eventually contributed to the CO_2 loss close to anode surface due to the acidic

environment at anode boundary layer region favoring dehydration of HCO_3^- to CO_2. From the

nucleation theory,[25,32] the CO_2 loss at the anode chamber was modeled as a volumetric source

term that was dependent on the CO_2 supersaturation (S) and a CO_2 loss coefficient (γ_{CO_2}) (see

equation S11). In addition, the CO_2 loss was experimentally measured in the gas mixture

evolving from the anode chamber using gas chromatography (see experimental method section in

the SI). Fig. 1b shows R_{CO_2A} as a function of operating current density at the cathode surface for

CO_2R. The anodic CO_2 loss due to crossover (R_{CO_2A}) can also be represented as an equivalent

loss in the CO_2R current density, which is defined as follows and shown in Fig. 1b:

$$j_{CO_2R,loss,eq} = nFR_{CO_2A} \qquad (2).$$

The simulation results show that R_{CO_2A} and $j_{CO_2R,loss,eq}$ increase linearly with increasing operating

current density at the cathode (dashed line in Fig. 1b). At the steady state, the simulation results

suggest that all the HCO_3^- ions that were crossing over the AEM contributed to the release of

CO_2 gas from the anode chamber. For instance, the rate of CO_2 loss of $R_{CO_2A} = 103$ nmol s^{-1}c

m^{-2} was a consequence of the HCO_3^- current density of $j_{HCO_3^-} = 9.9$ mA cm^{-2} crossing the

AEM at the operating current density of 10 mA cm^{-2}. The experimentally measured R_{CO_2A} (dots with error bars in Fig. 1b) at various operating current density were in close agreement with the simulation results confirming the mechanism of CO_2 loss in electrochemical or photoelectrochemical devices. Assuming the rate of the un-reacted CO_2 leaving the cathode chamber, R_{CO_2C} = 0 with ideal multi-pass reactor design, an upper limit of CO_2 utilization efficiency (η_{CO_2}) of 14.4% was found for all applied current densities for a 6-electron CO_2R reaction at the cathode (e.g., C_2H_4 or C_2H_5OH) in dependent of the operating current density of the device. The result suggests that in an aqueous-based CO_2R reactor with AEM, the CO_2 loss to the anode chamber is ~ 6 times higher than the CO_2 used and converted at the cathode. Note that the η_{CO_2} varies as the number of electrons per mole of CO_2 involved in CO_2R reaction changes. From Eq. 1 and Eq. 2, the calculated values of η_{CO_2} were 33.3%, 20%, and 11.1%, for 2-, 4-, and 8-electron CO_2R products, respectively (see Fig. 2a).

Fig. 1c shows the transient behavior of the rate of CO_2 gas release from the anode chamber. The green, blue, and red data points show the experimental CO_2 gas release rate as a function of time when the reactor operated at 10, 30 and 50 mA cm^{-2}, respectively. After the initial increase, the R_{CO_2A} and the corresponding $j_{CO_2R,loss,eq}$ reached to a steady-state value for all three current densities. Transport analysis of the cell was then carried out the understand the transient behavior as well as the spatial distribution of the CO_2 (g) release rates. Two values of the CO_2 releasing coefficient (γ_{CO_2}) were used and compared in this study, i.e.$\gamma_{CO_2} = 1.25 \times 10^{14}$ and 1.25×10^7 nmol s^{-1}cm^{-3}. While both values resulted in the same steady-state values of R_{CO_2A}, the former value (1.25×10^{14} nmol s^{-1}cm^{-3}), which was reported by Wilt[32], resulted in large discrepancy at the initial stage of the operation (0 - 60 minutes) shown as dashed lines in

Fig. 1c. By reducing the value of γ_{CO_2} to 1.25×10^7 nmol s^{-1}cm^{-3}, the transient behavior of the CO_2 gas release rate (Fig. 1c solid lines) matched relatively well with the experimental results. The CO_2 releasing coefficient (γ_{CO_2}) represented the gaseous CO_2 escaping rate (mol s^{-1}) per unit volume (m^{-3}) electrolyte. γ_{CO_2} is closely related to the nucleation rate of CO_2, which is highly dependent on the properties (roughness, wettability, etc) of the electrodes, the properties of electrolyte, and the operating current densities. The releasing coefficient also depends exponentially on the contact angle and the roughness of the surface where gas bubbles are nucleating. Wilt[32] showed that the rate of nucleation could vary over 7 orders of magnitude with changes in the surface roughness. In the present study, the lower value of CO_2 releasing coefficient is likely due to the smoother electrode surface with fewer sites to nucleate CO_2 bubbles. The simulations for all other reactors were performed with this corrected γ_{CO_2} value.

Fig. 1d shows the simulated spatial distribution of R_{CO_2A} as a function of distance from the anode surface. The R_{CO_2A} was significantly higher close to the anode surface and decreased drastically with the increasing distance from the anode surface, indicating a strong influence of pH on the nucleation of CO_2 gas in the aqueous electrolyte. The simulation results also suggested that the majority of the nucleation for CO_2 evolution occurred within ~1 μm distance from the anode surface, which agreed well with a previous study by Wilt and others.[32]

Figure 2a shows the effects of Faradaic efficiency (FE) and participation electron numbers for CO_2R reaction on the η_{CO2}. Higher FE and lower participation electron numbers exhibited higher η_{CO2}. For example, at an FE of 100% for a 2-electron CO_2RR, the η_{CO2} can reach up to 33.3% as compared to 14.4% for the reference case with a 100% FE and 6-electron CO_2RR. Note that the results are independent of operation current density according to eq. 1 as long as R_{CO2C} is equal

to 0 (ideal case for cathode gas recycling). In a more realistic case ($R_{CO2C} > 0$) when the cathode

gas recycling is not considered, the η_{CO_2} was much smaller (Fig. S3a). For example, a constant

CO_2 flow of 5 sccm is considered for a 1cm^2 area electrode undergoing 6-electron CO_2R reaction

with 100% FE, the maximum η_{CO_2} was 2.3% at an operating current density of 50 mA cm^{-2} (Fig.

S3a).

One approach to increase the η_{CO_2} is to reduce the CO_2 feed rate while keeping the same

operating current density for the cell. Figure 2b shows the R_{CO2A} and the corresponding η_{CO_2} as a

function of reduced cathode CO_2 feed rate at three different operating current densities. The CO_2

feed rate (R_{feed}) was defined as the following: $R_{feed} = f_{feed} \times k_{feed} \times c_{CO2}$, where the k_{feed} is 0.33 s^{-1}

based on literature data[25] corresponding to ~21 sccm for the 10 ml cathode chamber in this study,

and c_{CO2} is the electrolyte CO_2 concentration. The η_{CO_2} remained nearly constant (Fig. 2b) even

when the CO_2 feed rate was reduced by 10^4 times for all three operating current densities.

Further reduction of the CO_2 feed rate resulted in significant increase of the bulk pH of the

catholyte, a significant decrease of the dissolved CO_2 near the cathode electrode and lowering

the limiting current density of the cell (Fig. S3b) For instance, when the f_{feed} was reduced to

$<1.8 \times 10^{-4}$, the limiting current density of the cell was limited to < 50 mA cm^{-2}. In the extreme

case where f_{feed} was reduced to 1.5×10^{-5}, the bulk pH of the electrolyte reached to 10.1 in the

steady state operating and OH$^-$ contributed to the ionic transport through the AEM, a η_{CO_2} of 71.2%

was obtained at the limiting current density of the cell at 2.8 mA cm^{-2}. In addition, we also

showed that the CO_2 loss rate is independent of the spacing between the electrode and membrane

(see Fig. S4).

The R_{CO2A} in the AEM-based CO_2 reactor was mainly due to the dominating partial current

density of HCO$_3^-$ across the separator. One strategy to minimize the transference of HCO$_3^-$

across the AEM is to introduce supporting anions (current carriers) in the solution, such as adding a high concentration of buffers. Fig. 3 shows the experimental and modeling results of the R_{CO_2A} and the corresponding η_{CO_2} when 1 M phosphate buffer solution was added into various KHCO$_3$ (0.1, 0.5, and 1 M) solutions. The phosphate buffer species (H$_2$PO$_4^-$ and HPO$_4^{2-}$) were equilibrated according to its pKa of 6.9 in the CO$_2$-saturated solutions of pH=7.85 for 1 M KHCO$_3$, pH=7.55 for 0.5 M KHCO$_3$, and pH=6.58 for 0.1 M KHCO$_3$. The detailed buffer compositions are listed in Table S5 of the SI. The near neutral pH conditions used in this study were the dominating pH environments in reported CO$_2$R studies due to the lack of dissolved CO$_2$ in alkaline conditions (very low operating current density), and the poor selectivity for CO$_2$R in acidic conditions (very high selectivity towards HER).[25] In general, the reactors with buffered electrolytes exhibited higher CO$_2$ utilization efficiency for various concentrations of KHCO$_3$ solutions. The dashed green line and the dashed black line represent the simulated values of $j_{CO_2R,loss,eq}$ and the η_{CO_2} as a function of the HCO$_3^-$ concentration for the un-buffered, and buffered (1M phosphate buffer) solutions, respectively. The simulated η_{CO_2} increased from 14.4% to 15.9% in 1 M KHCO$_3$ solution when 1 M phosphate buffer electrolyte was added. The simulated η_{CO_2} was further increased up to ~24% by reducing the concentration of KHCO$_3$ to 0.1 M in a 1 M phosphate buffer solution. The experimentally measured $j_{CO_2R,loss,eq}$ and the corresponding η_{CO_2} (dots with error bar in Fig. 3a, also see transient data in Fig. S5a) showed a similar trend as compared to the simulation results. The measured η_{CO_2} was 14.4%, 19.6%, and 38.3% for 1 M, 0.5 M, and 0.1 M KHCO$_3$ case, respectively. The discrepancy between simulation and the experimental results with low bicarbonate concentrations could be due to the concentration-dependent diffusion coefficient of HCO$_3^-$ in AEM and in the buffered solutions (see SI and Fig. S6). To further understand the effect of buffer on the CO$_2$ crossover, spatial

distributions of the partial ionic current of various species were obtained at the steady state operation of the electrochemical CO_2R reactor. Fig. 3b shows the steady-state, spatial distribution of ionic current densities for all anions and cations in 1 M $KHCO_3$ solution with 1 M phosphate buffer at the operational current density of 30 mA cm^{-2}. The partial current density of cations- H^+ and K^+ were close to zero, whereas the anions have either positive or negative current density indicating the primary mechanism of transport being either migration or diffusion, respectively. The net current density of CO_2-carrier such as HCO_3^- and CO_3^{2-} was positive and in the direction away from the cathode.

The addition of a buffer reduces marginally the transference of HCO_3^-, while the majority of the current density across the AEM was still supported by HCO_3^- (red curve). The calculated partial current densities of HCO_3^-, CO_3^{2-}, $H_2PO_4^-$, and HPO_4^{2-}, were 26.5 mA cm^{-2}, 3.5 mA cm^{-2}, 2 mA cm^{-2}, and -2 mA cm^{-2}, respectively. As a result of a marginal reduction in the transference of HCO_3^-, negligible improvement in η_{CO_2} was observed when buffer electrolytes were added into the 1 M $KHCO_3$ solution. Substantial improvement in η_{CO_2} was observed by lowering the concentration of the $KHCO_3$ solution by an order of magnitude, which in turn, reduced the partial current density and transference of HCO_3^- across the AEM (see Fig. 3c). As seen in Fig. 3c, the partial current carried by $H_2PO_4^-$, and HPO_4^{2-} increased to 28.3 mA cm^{-2} and 13.9 mA cm^{-2} when reducing the $KHCO_3$ to 0.1 M while keeping the buffer solution concentration to be 1 M. This leads to reduced partial current densities of HCO_3^- and CO_3^{2-} (15.8 mA cm^{-2} and ~0 mA cm^{-2}) resulting in enhanced η_{CO_2}.

Another strategy to reduce the transference of HCO_3^- and hence the CO_2 loss is to use a CEM in the electrochemical CO_2R device. Fig. 4a shows the schematic illustration of an aqueous, CEM-

based CO_2R reactor.   Fig. 4 shows that although the CEM-based CO_2R reactors have the potential to minimize CO_2 crossover by blocking the HCO_3^- transport, the cell cannot be operated at steady-state without re-circulation due to the excessive potential losses associated with electrodialysis. Fig. 4b shows the experimentally measured values of the voltage drop due to the solution transport losses ($\Delta\phi_{solution}$) at two different current densities. The $\Delta\phi_{solution}$ increased as a function of time for both operating current densities until the cell potential exceeded the limit of the potentiostat (up to 11 V, see Fig. S7b). In the near neutral pH conditions, the K^+ was the dominating current carries across the CEM (see Fig S7a). While proton generation rate at the anode was the same as the K^+ crossover rate through the CEM, the proton generated at anode surface combined with carbonate ions to generate CO_2 that get escaped from the anolyte and mixed with the produced O_2 to the anode outlet. This leads to a decreased conductivity of anolyte resulting in continuous increase in cell voltage (see Fig. 4c) the increased pH gradients.[33] Fig. 4c shows the spatial distribution of all ionic species' concentrations (solid lines) and pH (black dash line) values across the CEM-based CO_2R reactor at an operating current density of 30 mA cm^{-2} at 400 minutes after the cell operation. The average concentration of K+ (c_{K+}) dropped below 0.01 M in anolyte, which resulted in the large electrolyte conductivity decrease and un-sustainable operation of the reactor. The nonlinear behavior of $\Delta\phi_{solution}$ as a function of the operation time was also a result of the reciprocal relation between transport loss and electrolyte conductivity (see eq. S15).   In principle, the depletion of the cation in the anolyte can be circumvented by convective re-circulation between the catholyte and anolyte.[34] However, the re-circulation and mixing between the catholyte and the anolyte would lead to a significant increase in R_{CO_2A} due to the effective transport of the dissolved CO_2 to the anode chamber (see Fig. S7c). The recirculation of electrolyte increased the value of R_{CO_2A} to 97 nmol s^{-1} cm^{-2}, and decreased

the corresponding η_{CO_2} to 15.1% at an operating current density of 10 mA cm^{-2} (Fig. S7c), which was comparable to the CO$_2$ loss in the AEM-based CO$_2$ reactor without recirculation.

To circumvent the electrodialysis loss in a CEM-based CO$_2$ reactor without re-circulation, a BPM can be used to facilitate the ion transport between the cathode and the anode, and to block the HCO$_3^-$ anion crossover to the anode. Fig. 5a shows the schematic illustration of the BPM-based CO$_2$R reactor. BPM is composed of a CEM component (colored orange) and an AEM (colored green) component. Instead of allowing specific ions to pass through the BPM, water was disassociated into H$^+$ and OH$^-$ at the BPM interface and transported to catholyte and anolyte through CEM and AEM layers, respectively. Fig. 5b shows the modeling (dashed lines) and the experimental measurements (dots) of the steady-state behavior of R_{CO_2A} and the corresponding η_{CO_2} at two different operating current densities – 30 and 50 mA cm^{-2}. The simulated R_{CO_2A} values at steady state conditions reached 32.4 and 40.9 nmol cm^{-2}s^{-1} for 30 and 50 mA cm^{-2}, respectively. Correspondingly, the experimentally measured R_{CO_2A} were 37.6 and 44.6 nmol cm^{-2}s^{-1} for 30 and 50 mA cm^{-2}(averaged value for the test range of 400 – 500 minutes), respectively, showing a reasonable agreement between simulation and experimental results. The transient behavior of $R_{CO_2A}$and the corresponding $j_{CO_2R,loss,eq}$can be found in Figure S8d. The CO$_2$ loss at steady state was driven primarily by the diffusion of the dissolved CO$_2$ across the BPM. A slightly higher R_{CO_2A}, which corresponds to a larger CO$_2$ concentration differential between the catholyte and anolyte, at higher operating current densities was observed because the higher release rate of CO$_2$ at the anode surface lowered averaged CO$_2$ concentration in anolyte. For example, the average CO$_2$ concentrations in the anolyte were 20.1 and 15 mM for 30 and 50 mA cm^{-2}, respectively. The η_{CO_2} in the BPM-based CO$_2$R reactor were 58.0% and 61.4% for 30 and 50 mA cm^{-2} for 6-electron CO$_2$R reaction, which was significantly higher than that of AEM-

based reactor (14.4%). Despite the improved η_{CO_2} in the BPM-based reactor compared to the AEM-based CO_2R reactor, the η_{CO_2} was still limited to 61.4% at the operating current density of 50 mA cm^{-2} (see Fig. 5b) for a 6 electron per mole of product CO_2R reaction. Further improvement in η_{CO_2} for the BPM-based reactor requires a reduction in the diffusion coefficient of dissolved CO_2 in BPM. Fig. 6 shows contour maps of the η_{CO_2} and the additional potential drop across BPM ($\Delta\phi_{membrane}$) as a function of the operating current density when a series of reduction factor of the CO_2 diffusion coefficient in BPM was used. The simulation results show that a reduction in the diffusion coefficient by 77 and 44 times were required to achieve η_{CO_2} of 90% for 10 and 50 mA cm^{-2}, respectively (see the solid line in Fig. 6a). Correspondingly, the additional potential drop across BPM ($\Delta\phi_{membrane}$) was relatively low (< 80 mV) to achieve a η_{CO_2} of 90% for a range of operating current densities from 10 to 50 mA cm^{-2} (see Fig. 6b). For a target η_{CO_2} of 70%, a reduction in the diffusion coefficient in BPM by 18 and 10 times were required for 10 and 50 mA cm^{-2}. This offers a practical design guideline for the design of BPM to achieve higher η_{CO_2}.

CONCLUSIONS

In summary, the CO_2 utilization efficiency in membrane-based electrochemical CO_2R reactors was quantitatively evaluated by modeling and experimental methods. The transport of the HCO_3^- across the AEM in AEM-based CO_2R reactors significantly limited the CO_2 utilization efficiency of the device. In AEM-based CO_2R reactors, an operating current density independent and an upper limit of 14.4% for the CO_2 utilization efficiency was observed by modeling and experiments in the CO_2 saturated aqueous electrolytes without any buffer electrolyte for 6-electron per mole of product CO_2R reaction with unity FE and ideal gas re-cycling. Lower Fes

15

and non-ideal gas recycling further lowered the CO_2 utilization efficiency in AEM-based CO_2R reactor. To operate at a current density of 10-50 mA cm^{-2} for solar-fuel devices, the reduction of the CO_2 feed in the cathode chamber did not improve the CO_2 utilization efficiency and started to limit the operating current density due to the increase of the bulk electrolyte pH. In the AEM-based reactor, the CO_2 utilization efficiency was improved from 14.4% to 38.3% when a 1 M of phosphate buffer solution was added in the 0.1 M bicarbonate solution. The CEM based CO_2R reactor exhibited low CO_2 utilization efficiency with re-circulation between the catholyte and the anolyte, and was unsustainable due to the cation depletion from the anolyte without any re-circulation. The BPM based CO_2R reactor operated continuously without any significant increase in the cell voltage and exhibited significantly higher CO_2 utilization efficiency, up to 61.4%, as compared to the AEM based CO_2R reactors. Further improvement in CO_2 utilization efficiency in the BPM-based reactor requires a reduction in the diffusion coefficient of CO_2 in the membrane. For example, η_{CO_2} of 90% can be achieved by reducing the CO_2 diffusion coefficient by ~77 times at 50 mA cm^{-2} without any significant increase in the voltage drop across the BPM. The study revealed significant challenges in CO2 utilization efficiency in aqueous-based electrochemical cells operating at current densities that are relevant to solar-fuel devices, and also provide design guidelines for membrane-based electrochemical or photoelectrochemical CO_2R reactors to achieve higher CO_2 utilization efficiencies.

CONFLICTS OF INEREST

There are no conflicts to declare.

SUPPORTING INFORMATION

The Supporting Information is available free of charge on the ACS Publications website at DOI: XXX, including: additional simulation results for AEM-, CEM-, BPM-based reactors; Transient CO_2 loss behavior for buffered AEM-based reactor; Transient behavior of reactor voltage for CEM-based reactor; Simulation method; and Experimental method.

NOTES AND REFERENCES

(1)   Li, K.; Peng, B.; Peng, T. Recent Advances in Heterogeneous Photocatalytic

CO2Conversion to Solar Fuels. *ACS Catal.* **2016**, *6* (11), 7485–7527.

https://doi.org/10.1021/acscatal.6b02089.

(2)   Zhou, X.; Liu, R.; Sun, K.; Chen, Y.; Verlage, E.; Francis, S. A.; Lewis, N. S.; Xiang, C.

Solar-Driven Reduction of 1 Atm of CO2 to Formate at 10% Energy-Conversion

Efficiency by Use of a TiO2-Protected III–V Tandem Photoanode in Conjunction with a

Bipolar Membrane and a Pd/C Cathode. *ACS Energy Lett.* **2016**, *1* (4), 764–770.

https://doi.org/10.1021/acsenergylett.6b00317.

(3)   Jouny, M.; Luc, W.; Jiao, F. High-Rate Electroreduction of Carbon Monoxide to Multi-

Carbon Products. *Nat. Catal.* **2018**, *1* (10), 748. https://doi.org/10.1038/s41929-018-0133-

2.

(4)   Dinh, C. T.; Burdyny, T.; Kibria, G.; Seifitokaldani, A.; Gabardo, C. M.; Pelayo García

De Arquer, F.; Kiani, A.; Edwards, J. P.; De Luna, P.; Bushuyev, O. S.; Zou, C.; Quintero-

Bermudez, R.; Pang, Y.; Sinton, D.; Sargent, E. H. CO2 Electroreduction to Ethylene via

Hydroxide-Mediated Copper Catalysis at an Abrupt Interface. *Science (80-.).* **2018**, *360*

(6390), 783–787. https://doi.org/10.1126/science.aas9100.

(5)   Jhong, H. R. M.; Ma, S.; Kenis, P. J. Electrochemical Conversion of CO2to Useful

Chemicals: Current Status, Remaining Challenges, and Future Opportunities. *Curr. Opin.*

Chem. Eng. **2013**, *2* (2), 191–199. https://doi.org/10.1016/j.coche.2013.03.005.

(6)   Zhuang, T.-T.; Pang, Y.; Liang, Z.-Q.; Wang, Z.; Li, Y.; Tan, C.-S.; Li, J.; Dinh, C. T.; De

Luna, P.; Hsieh, P.-L.; Burdyny, T.; Li, H.-H.; Liu, M.; Wang, Y.; Li, F.; Proppe, A.;

Johnston, A.; Nam, D.-H.; Wu, Z.-Y.; Zheng, Y.-R.; Ip, A. H.; Tan, H.; Chen, L.-J.; Yu,

S.-H.; Kelley, S. O.; Sinton, D.; Sargent, E. H. Copper Nanocavities Confine Intermediates for Efficient Electrosynthesis of C3 Alcohol Fuels from Carbon Monoxide. *Nat. Catal.* **2018**, *1* (12), 946–951. https://doi.org/10.1038/s41929-018-0168-4.

(7)   Zhou, Y.; Che, F.; Liu, M.; Zou, C.; Liang, Z.; De Luna, P.; Yuan, H.; Li, J.; Wang, Z.; Xie, H.; Li, H.; Chen, P.; Bladt, E.; Quintero-Bermudez, R.; Sham, T. K.; Bals, S.; Hofkens, J.; Sinton, D.; Chen, G.; Sargent, E. H. Dopant-Induced Electron Localization Drives CO2reduction to C2hydrocarbons. *Nat. Chem.* **2018**, *10* (9), 974–980. https://doi.org/10.1038/s41557-018-0092-x.

(8)   Cook, R. L. High Rate Gas Phase CO2 Reduction to Ethylene and Methane Using Gas Diffusion Electrodes. *J. Electrochem. Soc.* **1990**, *137* (2), 607. https://doi.org/10.1149/1.2086515.

(9)   Lu, Q.; Jiao, F. Electrochemical CO2 Reduction: Electrocatalyst, Reaction Mechanism, and Process Engineering. *Nano Energy* **2016**, *29*, 439–456. https://doi.org/10.1016/j.nanoen.2016.04.009.

(10) Yang, H. Bin; Hung, S. F.; Liu, S.; Yuan, K.; Miao, S.; Zhang, L.; Huang, X.; Wang, H. Y.; Cai, W.; Chen, R.; Gao, J.; Yang, X.; Chen, W.; Huang, Y.; Chen, H. M.; Li, C. M.; Zhang, T.; Liu, B. Atomically Dispersed Ni(i) as the Active Site for Electrochemical CO2 Reduction. *Nat. Energy* **2018**, *3* (2), 140–147. https://doi.org/10.1038/s41560-017-0078-8.

(11) Jiang, K.; Siahrostami, S.; Zheng, T.; Hu, Y.; Hwang, S.; Stavitski, E.; Peng, Y.; Dynes, J.; Gangisetty, M.; Su, D.; Attenkofer, K.; Wang, H. Isolated Ni Single Atoms in Graphene Nanosheets for High-Performance CO2reduction. *Energy Environ. Sci.* **2018**, *11* (4), 893–903. https://doi.org/10.1039/c7ee03245e.

(12) Weekes, D. M.; Salvatore, D. A.; Reyes, A.; Huang, A.; Berlinguette, C. P. Electrolytic

CO2 Reduction in a Flow Cell. *Acc. Chem. Res.* **2018**, *51* (4), 910–918.

(13)   Zhu, S.; Jiang, B.; Cai, W.-B.; Shao, M. Direct Observation on Reaction Intermediates and

the Role of Bicarbonate Anions in CO2 Electrochemical Reduction Reaction on Cu

Surfaces. *J. Am. Chem. Soc.* **2017**, *139* (44), 15664–15667.

(14)   Verma, S.; Lu, X.; Ma, S.; Masel, R. I.; Kenis, P. J. A. The Effect of Electrolyte

Composition on the Electroreduction of CO2 to CO on Ag Based Gas Diffusion

Electrodes. *Phys. Chem. Chem. Phys.* **2016**, *18* (10), 7075–7084.

https://doi.org/10.1039/c5cp05665a.

(15)   Han, L.; Zhou, W.; Xiang, C. High-Rate Electrochemical Reduction of Carbon Monoxide

to Ethylene Using Cu-Nanoparticle-Based Gas Diffusion Electrodes. *ACS Energy Lett.*

2018, *3* (4), 855–860. https://doi.org/10.1021/acsenergylett.8b00164.

(16)   Lv, J.; Jouny, M.; Luc, W.; Zhu, W.; Zhu, J.; Jiao, F. A Highly Porous Copper

Electrocatalyst for Carbon Dioxide Reduction. *Adv. Mater.* **2018**, *30* (49), 1803111.

https://doi.org/10.1002/adma.201803111.

(17)   Li, Y. C.; Zhou, D.; Yan, Z.; Gonçalves, R. H.; Salvatore, D. A.; Berlinguette, C. P.;

Mallouk, T. E. Electrolysis of CO2 to Syngas in Bipolar Membrane-Based

Electrochemical Cells. *ACS Energy Lett.* **2016**, *1* (6), 1149–1153.

(18)   Vermaas, D. A.; Smith, W. A. Synergistic Electrochemical CO2 Reduction and Water

Oxidation with a Bipolar Membrane. *ACS Energy Lett.* **2016**, *1* (6), 1143–1148.

(19)   Vermaas, D. A.; Wiegman, S.; Nagaki, T.; Smith, W. A. Ion Transport Mechanisms in

Bipolar Membranes for (Photo) Electrochemical Water Splitting. *Sustain. Energy Fuels*

2018, *2* (9), 2006–2015.

(20)   Salvatore, D. A.; Weekes, D. M.; He, J.; Dettelbach, K. E.; Li, Y. C.; Mallouk, T. E.;

Berlinguette, C. P. Electrolysis of Gaseous CO2 to CO in a Flow Cell with a Bipolar

Membrane. *ACS Energy Lett.* **2017**, *3* (1), 149–154.

(21)   Schreier, M.; H?roguel, F.; Steier, L.; Ahmad, S.; Luterbacher, J. S.; Mayer, M. T.; Luo, J.;

Gr?tzel, M. Solar Conversion of CO2 to CO Using Earth-Abundant Electrocatalysts

Prepared by Atomic Layer Modification of CuO. *Nat. Energy* **2017**, *2* (June), 17087.

https://doi.org/10.1038/nenergy.2017.87.

(22)   Zhou, X.; Liu, R.; Sun, K.; Chen, Y.; Verlage, E.; Francis, S. A.; Lewis, N. S.; Xiang, C.

Solar-Driven Reduction of 1 Atm of CO2 to Formate at 10% Energy-Conversion

Efficiency by Use of a TiO2-Protected III-V Tandem Photoanode in Conjunction with a

Bipolar Membrane and a Pd/C Cathode. *ACS Energy Lett.* **2016**, *1* (4), 764–770.

https://doi.org/10.1021/acsenergylett.6b00317.

(23)   Gurudayal; Bullock, J.; Srankó, D. F.; Towle, C. M.; Lum, Y.; Hettick, M.; Scott, M. C.;

Javey, A.; Ager, J. Efficient Solar-Driven Electrochemical CO 2 Reduction to

Hydrocarbons and Oxygenates. *Energy Environ. Sci.* **2017**, *10* (10), 2222–2230.

https://doi.org/10.1039/c7ee01764b.

(24)   Gurudayal; Beeman, J. W.; Bullock, J.; Wang, H.; Eichhorn, J.; Towle, C.; Javey, A.;

Toma, F. M.; Mathews, N.; Ager, J. W. Si Photocathode with Ag-Supported Dendritic Cu

Catalyst for CO2 Reduction. *Energy Environ. Sci.* **2019**, *12* (3), 1068–1077.

https://doi.org/10.1039/c8ee03547d.

(25)   Singh, M. R.; Clark, E. L.; Bell, A. T. Effects of Electrolyte, Catalyst, and Membrane

Composition and Operating Conditions on the Performance of Solar-Driven

Electrochemical Reduction of Carbon Dioxide. *Phys. Chem. Chem. Phys.* **2015**, *17* (29),

18924–18936. https://doi.org/10.1039/c5cp03283k.

(26)   Chen, Y.; Lewis, N. S.; Xiang, C. Modeling and Simulation of the Spatial and Light-Intensity Dependence of Product Distributions in an Integrated Photoelectrochemical CO2 Reduction System. *ACS Energy Lett.* **2016**, *1* (1), 273–280. https://doi.org/10.1021/acsenergylett.6b00134.

(27)   Hashiba, H.; Weng, L. C.; Chen, Y.; Sato, H. K.; Yotsuhashi, S.; Xiang, C.; Weber, A. Z. Effects of Electrolyte Buffer Capacity on Surface Reactant Species and the Reaction Rate of CO2in Electrochemical CO2reduction. *J. Phys. Chem. C* **2018**, *122* (7), 3719–3726. https://doi.org/10.1021/acs.jpcc.7b11316.

(28)   Li, Y. C.; Yan, Z.; Hitt, J.; Wycisk, R.; Pintauro, P. N.; Mallouk, T. E. Bipolar Membranes Inhibit Product Crossover in CO2 Electrolysis Cells. *Adv. Sustain. Syst.* **2018**, *2* (4), 1700187. https://doi.org/10.1002/adsu.201700187.

(29)   Arai, T.; Sato, S.; Morikawa, T. A Monolithic Device for CO2 Photoreduction to Generate Liquid Organic Substances in a Single-Compartment Reactor. *Energy Environ. Sci.* **2015**, *8* (7), 1998–2002. https://doi.org/10.1039/c5ee01314c.

(30)   Sugano, Y.; Ono, A.; Kitagawa, R.; Tamura, J.; Yamagiwa, M.; Kudo, Y.; Tsutsumi, E.; Mikoshiba, S. Crucial Role of Sustainable Liquid Junction Potential for Solar-to-Carbon Monoxide Conversion by a Photovoltaic Photoelectrochemical System. *RSC Adv.* **2015**, *5* (67), 54246–54252. https://doi.org/10.1039/c5ra07179h.

(31)   Jeon, H. S.; Koh, J. H.; Park, S. J.; Jee, M. S.; Ko, D.-H.; Hwang, Y. J.; Min, B. K. A Monolithic and Standalone Solar-Fuel Device Having Comparable Efficiency to Photosynthesis in Nature. *J. Mater. Chem. A* **2015**, *3* (11), 5835–5842. https://doi.org/10.1039/c4ta06495j.

(32)   Wilt, P. M. Nucleation Rates and Bubble Stability in Water-Carbon Dioxide Solutions. *J.*

Colloid Interface Sci. **1986**, *112* (2), 530–538.

(33)   Singh, M. R.; Papadantonakis, K.; Xiang, C.; Lewis, N. S. An Electrochemical

Engineering Assessment of the Operational Conditions and Constraints for Solar-Driven

Water-Splitting Systems at near-Neutral PH. *Energy Environ. Sci.* **2015**, *8* (9), 2760–2767.

https://doi.org/10.1039/c5ee01721a.

(34)   Singh, M. R.; Xiang, C.; Lewis, N. Evaluation of Flow Schemes for Near-Neutral

Electrolytes in Solar-Fuels Generators. *Sustain. Energy Fuels* **2017**, *1*, 458–466.

https://doi.org/10.1039/C7SE00062F.
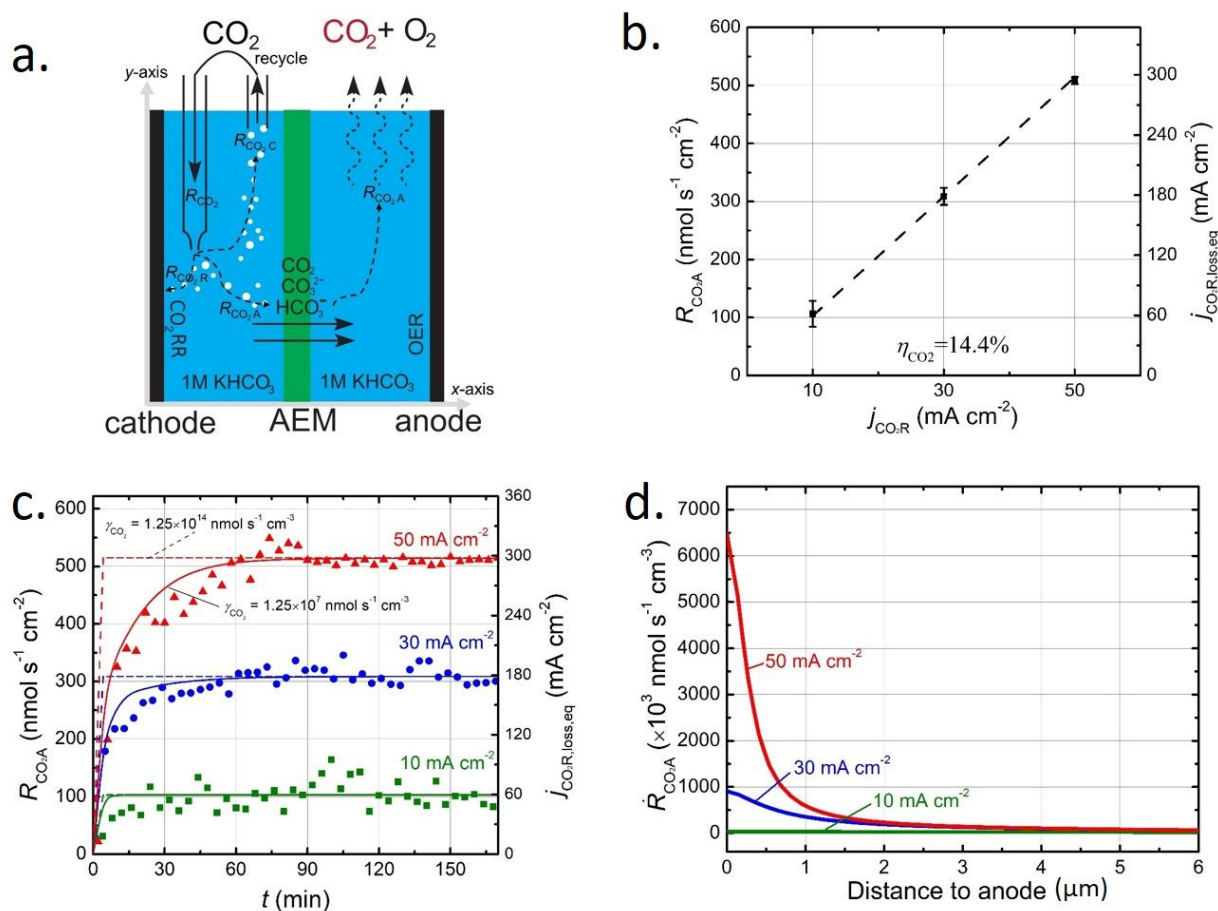
Figure 1. (a) A schematic illustration of the AEM based CO_2R reactor. (b) The CO_2 loss rate (R_{CO_2A}) and the equivalent CO_2 current density loss ($j_{CO_2R,loss,eq}$) as a function of operating current density. (c) Transient behavior of R_{CO_2A} and $j_{CO_2R,loss,eq}$ of AEM cell for different operating current densities (50 mA cm^{-2} in red, 30 mA cm^{-2} in blue, and 10 mA cm^{-2} in green) with two CO_2 releasing coefficients (γ_{CO_2}). (d) Volumetric CO_2 (R_{CO_2A}) loss rate distribution as a function of distance from anode to cathode surfaces for applied current densities of 10, 30, and 50 mA cm^{-2}. Dots with error bars are experimental data and solid and dashed line are simulation data. The 1D simulation is performed along the *x*-axis.
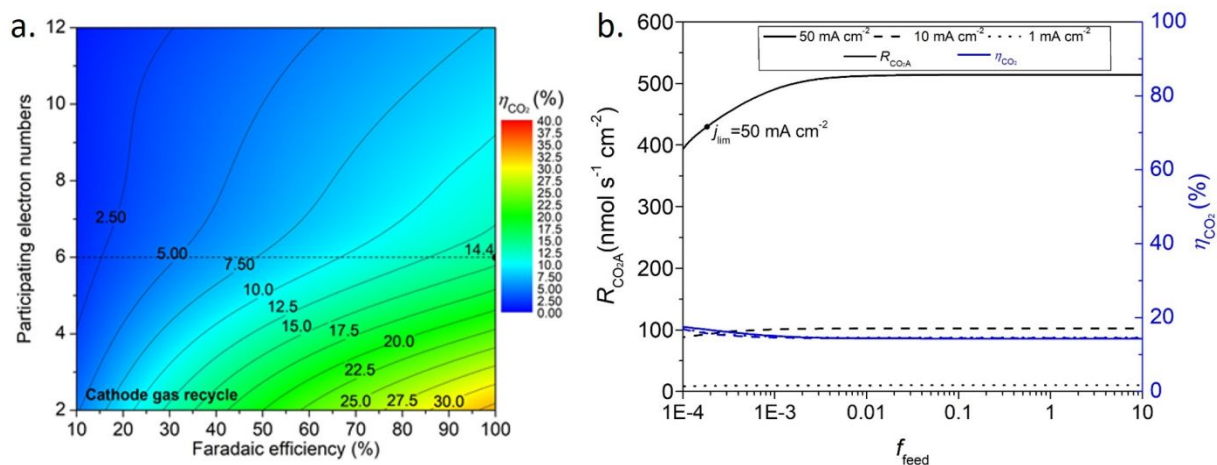
Figure 2. (a) The CO_2 utilization efficiency (η_{CO2}) as a function of CO_2R participating electron numbers and Faradaic efficiency without considering R_{CO2C} (cathode gas recycle). (b) R_{CO2A} and η_{CO2} as a function of reduced cathode CO_2 feed rate by a factor of f_{feed} at operating current density of 1, 10, and 50 mA cm^{-2}
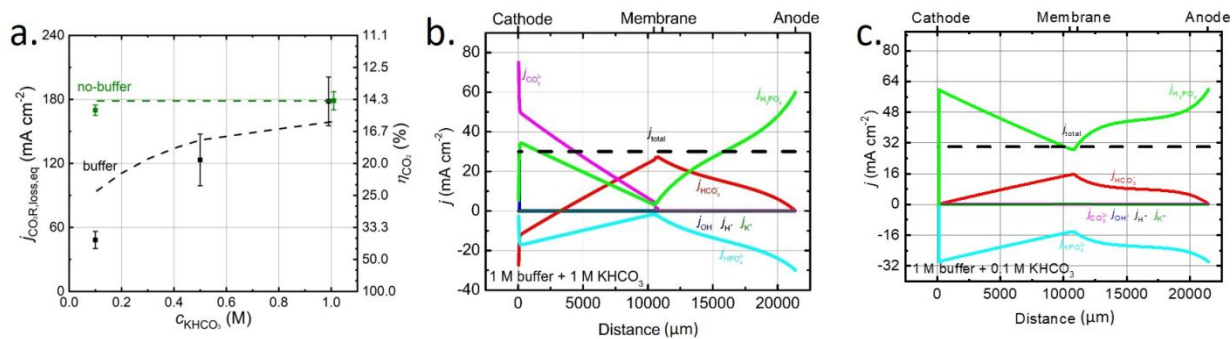
Figure 3. (a) $j_{CO_2R,loss,eq}$ and η_{CO_2} as a function of KHCO$_3$ concentration with 1 M phosphate buffer solution for at an operating current density of 30 mA cm^{-2}. The no-buffer case (0.1M and 1M KHCO$_3$) was plotted in green as a reference. Dots with error bars are experimental data and lines are simulation data. (b) Partial current density as a function of distance from the cathode surface for the case with 1 M KHCO$_3$ and 1 M phosphate buffer solution under an applied current density of 30 mA cm^{-2} at steady state condition. (c) Partial current density as a function of distance from the cathode surface for the case with 0.1 M KHCO$_3$ and 1 M phosphate buffer solution under an applied current density of 30 mA cm^{-2} at steady state condition.
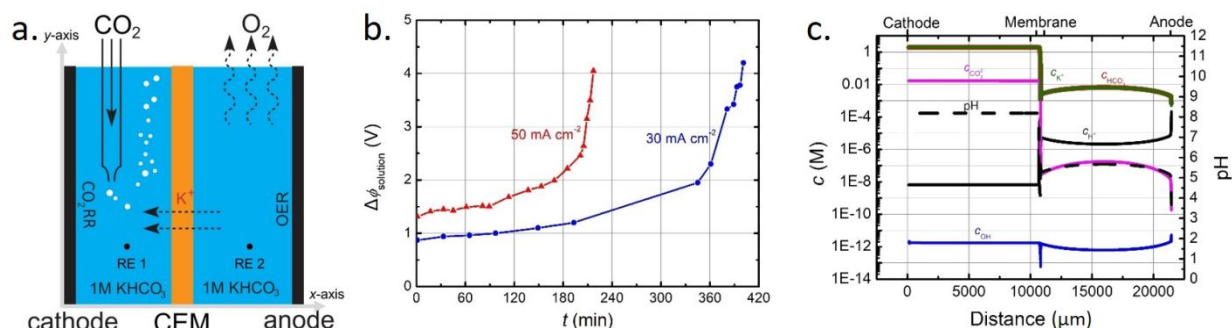
Figure 4. (a) A schematic illustration of the CEM based CO_2R reactor. Two reference electrodes (RE 1 and RE 2, black dots) were placed at the middle of cathode and anode for the quantification of the voltage drop across separator and electrolyte. (b) Experimentally measured voltage loss due to mass transport in the electrolyte and CEM (voltage difference between two reference electrodes) as a function of time for the applied current densities of 30 mA cm^{-2} (in blue) and 50 mA cm $^{-2}$ (in red). (c) Species concentration and pH as a function of distance from the cathode surface for the case for the applied current density of 30 mA cm^{-2} at $\Delta\phi_{solution}$ = 4 V.
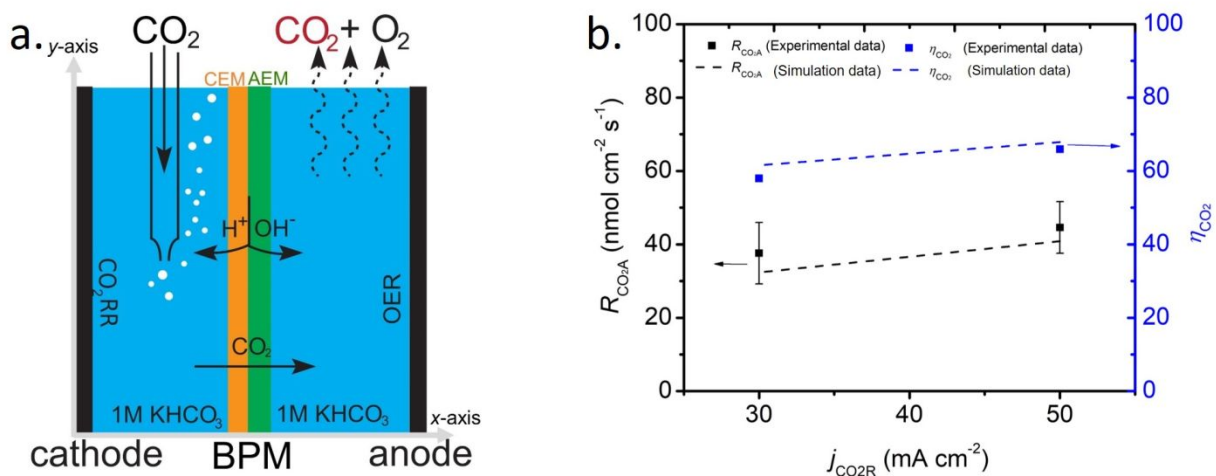
Figure 5. (a) A schematic illustration of the BPM based CO_2R reactor with 1 M $KHCO_3$. (b) R_{CO_2A} and the corresponding η_{CO_2} as a function of the operating current density for both experimental data (dots) and simulation data (dash lines).
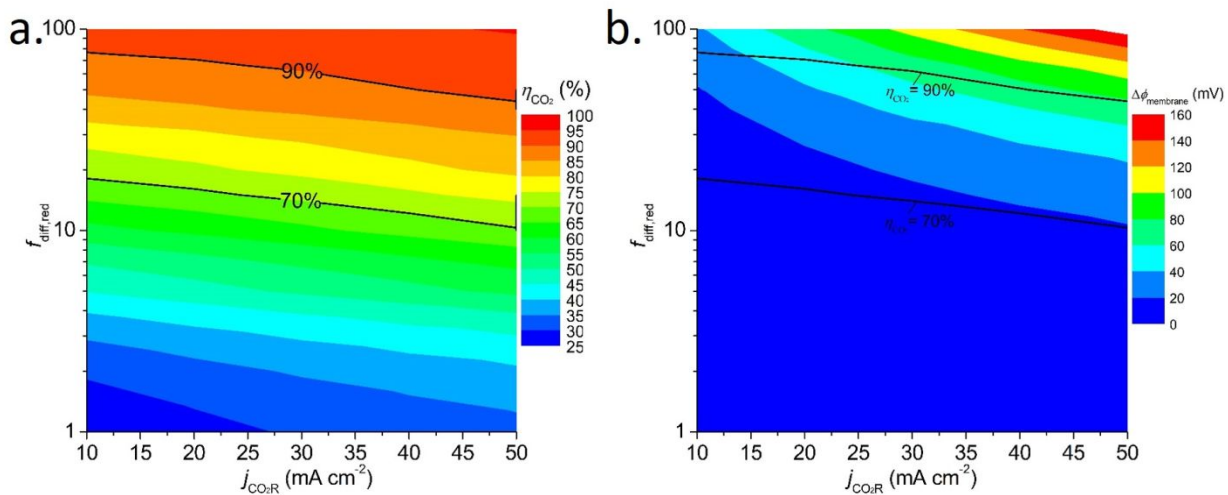
Figure 6. (a) Contour map of η_{CO_2} as a function of CO_2 (aq) diffusion coefficient reduction factor ($f_{diff,red}$) and j_{CO_2R} for the BPM-based CO_2R reactor. (b) Contour map of $\Delta\phi_{membrane}$ as a function of CO_2 (aq) diffusion coefficient reduction factor ($f_{diff,red}$) and j_{CO_2R} for the BPM-based CO_2R reactor.